ADVANCED ENERGY & SUSTAINABILITY RESEARCH
Open Access
www.advenergysustres.com

Sodium-Containing Surface Film Formation on Planar Metal–Oxide Electrodes with Potential Application for Sodium-Ion and Sodium–Oxygen Batteries

*Lukas Szabados, Daniel Winkler, David Stock, Thöny Alexander, Thomas Lörting, Julia Kunze-Liebhäuser, and Engelbert Portenkirchner**

Excellent, self-improving sodiation rate capabilities in combination with high capacity retention upon galvanostatic charge/discharge cycling are found for oxygen-deficient, carburized, and self-organized titanium dioxide (TiO_{2-x}) nanotubes (NTs). The sodiation mechanism is attributed to the formation of an acicular surface film as the active storage material with sodium (Na) peroxide (Na_2O_2) being the main component. Whether the proposed surface chemistry is unique for TiO_2 NTs or serves as a common scheme for Na-ion storage at metal oxide surfaces, in general, is not clear by now. Herein, three different materials, titanium(IV) oxide in the anatase and rutile phase and molybdenum(IV) oxide, are investigated in a planar electrode geometry toward their capability for Na-ion storage. It is shown that all three materials under investigation demonstrate a significant progression of capacity increase upon cycling in combination with the formation of a Na-oxide containing surface film. These "self-improving" characteristics are found to significantly enhance the Na-ion storage performance of the electrodes during long-term galvanostatic cycling in a Na-containing electrolyte.

1. Introduction

Storage of intermittent, renewable energy is considered key for mitigating the issues related to manmade global warming.[1–3] Particularly rechargeable batteries are found to be an ideal storage technology for electrical energy and became indispensable in numerous applications, starting from small-scale electronic devices to power-demanding electric vehicles.[4,5] The predominant lithium (Li)-ion battery (LIB) has raised concerns mainly due to its environmentally harmful mining and its limited availability, resulting in substantial increase in the price of Li.[6] Consequently, alternative battery technologies based on sodium (Na) over Li have drawn great interest in recent years, mainly motivated by the high natural abundance of Na.[7–9] Encouraging progress on conversion/alloying-based metal anode materials, that demonstrate rapid and stable Na-ion storage,[10,11] invites future exploration of the Na-ion storage mechanism.

We were able to show that electrochemically grown, oxygen-deficient, carburized, and self-organized TiO_{2-x}-C nanotubes (NTs) are capable of substantial Na-ion storage in the range of $202.2 \pm 50.6\,\text{mAh g}^{-1}$ at a current rate of $30\,\text{mA g}^{-1}$ (C/20), that self-improves as cycling proceeds.[12] The prevailing Na-ion storage mechanism has been elucidated in a previous publication, showing that alongside organic species from the decomposition of the electrolyte, mainly inorganic compounds, such as Na_2O_2 and $NaCO_3$, with a characteristic acicular morphology, are the main constituents.[13] The formation of Na_2O_2 upon sodiation and its conversion to sodium superoxide (NaO_2) upon desodiation are characterized by pseudocapacitive charge storage characteristics, allowing excellent rate capabilities and storage capacities measured for TiO_{2-x}-C NTs.[12,13] This is particularly interesting since the initial discharge product in sodium–oxygen batteries is shown to be NaO_2, which undergoes dissolution and then transforms to Na_2O_2 and Na_2O_2 dihydrate.[14–16]

Whether the proposed formation of NaO_2 and Na_2O_2 at the electrodes surface upon sodiation is unique for TiO_2 NTs or can generally be seen as common characteristics for Na-ion storage at metal oxide surfaces are yet to be clarified. To address this important open question, we investigate in this work three different transition metal oxides, namely, titanium(IV) oxide in the two polymorphous forms of anatase (TiO_2-A) and rutile (TiO_2-R) and molybdenum(IV) oxide, toward their capability for Na-ion storage. Molybdenum dioxide (MoO_2) has been suggested as a promising anode material for LIBs and sodium-ion

L. Szabados, D. Winkler, T. Alexander, T. Lörting, J. Kunze-Liebhäuser, E. Portenkirchner
Institute of Physical Chemistry
University of Innsbruck
6020 Innsbruck, Austria
E-mail: Engelbert.Portenkirchner@uibk.ac.at

D. Stock
Institut für Konstruktion und Materialwissenschaften
University of Innsbruck
A-6020 Innsbruck, Austria

The ORCID identification number(s) for the author(s) of this article can be found under https://doi.org/10.1002/aesr.202200104.

DOI: 10.1002/aesr.202200104

batteries (SIBs) owing to its high electrical conductivity (1.9×10^2 S cm^{-1}) and good chemical stability.[17] The two different TiO_2 polymorphs are chosen to investigate the influence of oxygen diffusivity on the surface film formation characteristics, which is considered crucial for the suggested Na-ion storage mechanism. The oxygen diffusivity has been reported to be markedly different in anatase and rutile TiO_2.[18–20] To exclude morphological issues arising from a nanostructured surface, like in the previously reported TiO_{2-x}-C NTs,[12,13] a planar electrode geometry is used for all electrodes in this study.

The phase purity of the electrodes is investigated by Raman and quasi in situ X-ray photoelectron spectroscopy (XPS) analysis.[21] The electrodes are further characterized electrochemically in a SIB half-cell setup by potential-dependent impedance spectroscopy, cyclic voltammetry (CV) measurements, and galvanostatic cycling with potential limitation (GCPL). Finally, postmortem analysis using XPS and scanning electron microscopy (SEM) in combination with energy-dispersive X-ray (EDX) mapping are employed to examine the composition and morphology of potential surface films formed during battery half-cell cycling. Our findings show that all three materials under investigation are characterized by a significant capacity increase upon cycling, coming along with the formation of a Na-containing surface film. This "self-improving" characteristics enhance the performance of the electrodes during long-term GCPL measurements in both, the specific gravimetric Na-ion storage capacity and their sodiation/desodiation rate capability.

2. Results and Discussion

Titanium(IV) oxide electrodes are synthesized by electrochemical oxidation of the parent Ti–metal substrate and, for synthesis of the anatase phase (TiO_{2-x}-A), by subsequent phase transition upon thermal annealing in a tube furnace.[22] Molybdenum(IV) oxide (MoO_{2+x}) electrodes are prepared by radio frequency magnetron sputtering of molybdenum in oxygen/argon gas mixture on copper (Cu) substrates. Raman (Figure S1, Supporting Information), XPS (Figure S2, Supporting Information), X-ray diffractograms (XRD, Figure S3, Supporting Information), and SEM (**Figure 1**) measurements were performed to confirm the successful preparation of the electrodes and investigate their surface structure, chemistry, the crystalline phase, and morphology. To calculate the active electrode mass and thereupon the C-rates, the exact thicknesses of the oxide layers are determined by cross-section SEM imaging (Figure 1).

The TiO_{2-x}-A layer is uniform on top of the parent Ti metal substrate (Figure 1a) and characterized by an average layer thickness of about 250 nm (exactly: 248 ± 28 nm, Figure 1b). The oxide layer has surface irregularities due to the texture and defects of the polycrystalline material. In contrast, the sputtered MoO_{2+x} film on top of the copper substrate (Figure 1d) appears uniform and smooth with an average layer thickness of about 210 nm (exactly 209 ± 10 nm, Figure 1e).

2.1. Cyclic Voltammetry

For initial electrochemical characterization, CV measurements are conducted in a Na-ion containing, carbonate-based electrolyte (see Experimental Section). **Figure 2** shows the current response as a function of the electrode potential of three different metal–oxide electrodes before (initial) and after 310 (aged) galvanostatic sodiation/desodiation cycles at different C rates (**Figure 3**).

Besides a significant cathodic current increase at potentials below 0.5 V, no distinct features that are related to Na-ion storage are visible in the initial CVs of the pristine electrodes, before aging (Figure 2, black lines). After galvanostatic

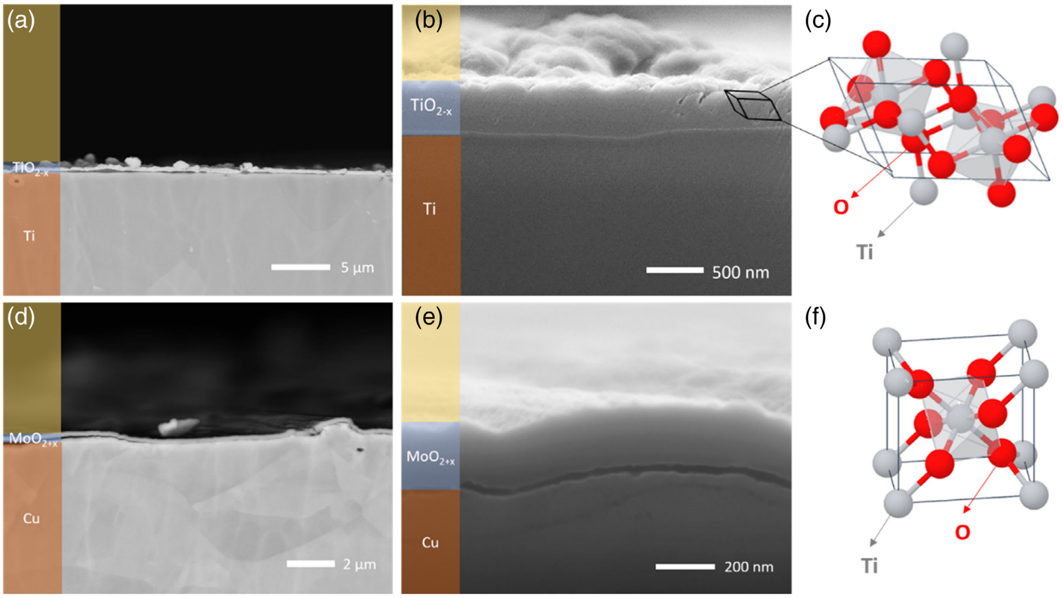

Figure 1. Metal–oxide surface film morphology. Cross-section SEM images of the oxide film formed at synthesized TiO_{2-x}-A a) overview and b) zoom and MoO_{2+x} c) overview and d) zoom electrodes. The different layers are color highlighted and labeled on the left side. Illustration of the crystal structure of c) tetragonal anatase and f) rutile TiO_2, respectively.

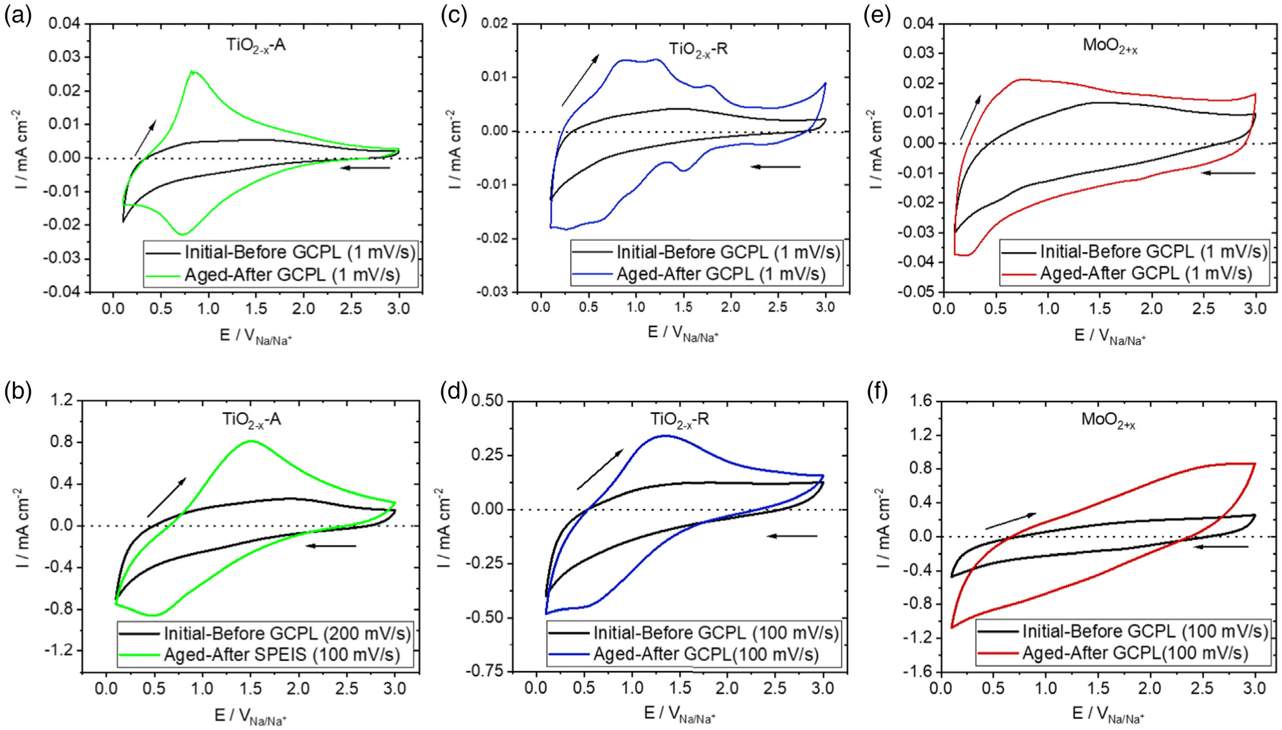

Figure 2. Electrochemical characterization. CV measurements for the initial and aged (after 310 GCPL cycles) electrodes of a,b) TiO_{2-x}-A, c,d) TiO_{2-x}-R, and e,f) MoO_{2+x} between 3.0 and 0.1 V for a scan rate of 1 and 100 mV s^{-1}.

sodiation/desodiation cycling, however, broad anodic and cathodic peaks occur for both, slow and fast scan rates of 1 and 100 mV s^{-1} in the TiO_{2-x} electrodes. The aged samples of TiO_{2-x}-A (Figure 2a,b) exhibit a prominent anodic and cathodic peak pair at 1 mV s^{-1}, located at 0.85 and 0.73 V, respectively. At faster scan rates of 100 mV s^{-1}, this peak pair broadens, showing a lager voltage hysteresis with its peak maxima at 1.51 and 0.48 V, respectively. These characteristics are perfectly in line with the previously reported surface reactions upon sodiation of aged anatase TiO_2 NTs, that lead to the formation of Na_2O_2-containing surface films reversibly formed and dissolved during sodiation and desodiation.[13] The CV response of aged TiO_{2-x}-R (Figure 2c,d) is more complex at slow scan rates of 1 mV s^{-1}, showing at least three different oxidation peaks at 0.85, 1.20, and 1.76 V, as well as four peaks at 0.26, 0.65, 0.98, and 1.50 V in the reduction regime. Since all of these signals are not present in the initial TiO_{2-x}-R electrode before GCPL cycling, they can be attributed to different redox reactions related to the formed surface film. Although rutile- and anatase-structured TiO_2 have the same chemical composition, the differences in the coordination environments, and hence chemical bonding, result in very different defect kinetics and surface states.[18] Accordingly, O-vacancy diffusion characteristics and charge transfer energy barriers are affected and may form various inorganic species such as sodium superoxide (NaO_2) or sodium carbonate (Na_2CO_3), in addition to Na_2O_2, which can contribute to the complex CV response for the aged TiO_{2-x}-R at slow scan rates (1 mV s^{-1}). At faster scan rates of 100 mV s^{-1}, the CV response of TiO_{2-x}-R is similar to that of TiO_{2-x}-A, with only one broad peak pair located at 1.34 and 0.52 V, respectively. Consequently, at faster scan rates, a similar redox chemistry as for the TiO_{2-x}-A electrode can be envisaged for the TiO_{2-x}-R electrode.

The CV response of the initial MoO_{2+x} electrode (Figure 2e, black line) shows a small, broad cathodic peak at around 0.52 V which is, as previously reported, most likely due to the initial formation of a solid–electrolyte interphase (SEI).[23] For the aged MoO_{2+x} electrode (Figure 2e, red line) an ill-defined, broad redox wave is located at around 0.2 and 0.72 V, respectively. The exact Na storage in MoO_2 is still under debate in literature. Reports suggest, similar to previous studies using a Li-containing electrolyte,[24] an initial sodiation of the topmost MoO_2 layers, according to Equation (1)[17]

$$MoO_2 + xNa^+ + xe^- \rightleftharpoons Na_xMoO_2 \qquad (1)$$

When cycling is continued to lower potentials, that is, 0.1 V versus Na/Na^+, it is proposed that the initially formed Na_xMoO_2 and residual MoO_2 are converted to metallic Mo and Na_2O, according to Equation (2) and (3)[25]

$$Na_xMoO_2 \rightleftharpoons Mo^0 + \frac{x}{2}Na_2O \qquad (2)$$

$$MoO_2 + 4Na^+ + 4e^- \rightleftharpoons Mo^0 + 2Na_2O \qquad (3)$$

The reversible formation of metallic Mo and Na_2O, however, has still to be verified.[23] This is especially interesting, as our previous study on Na-ion storage at TiO_{2-x}-A electrodes revealed the formation of Na_2O_2 upon sodiation and its conversion to

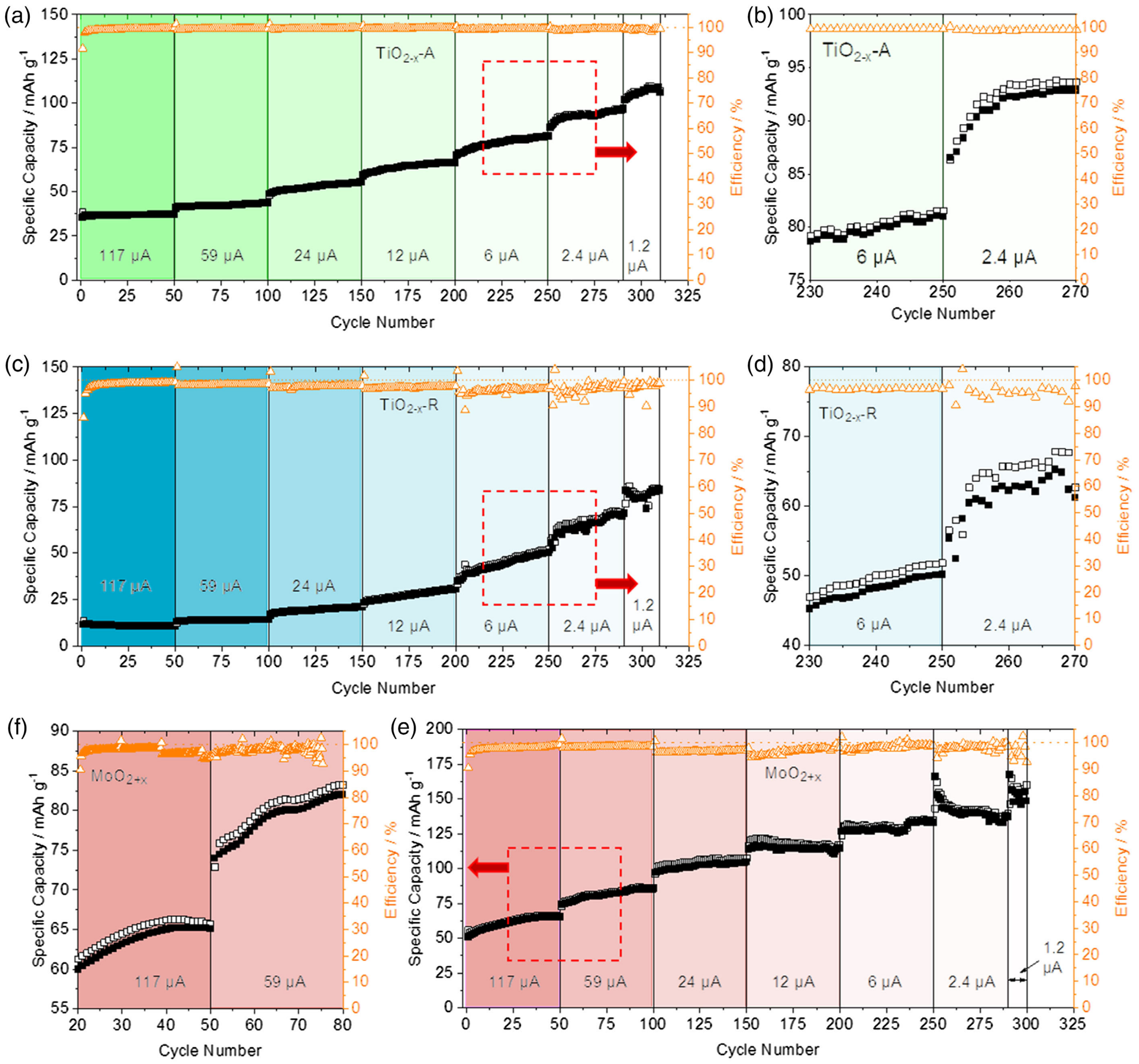

Figure 3. Self-improving charge storage characteristics. The specific gravimetric capacities (black squares) with respect to the cycle number and corresponding Coulombic efficiencies (orange triangles) of a) TiO_{2-x}-A, c) TiO_{2-x}-R, and e) MoO_{2+x}. Closed squares relate to charge (desodiation) and open squares to discharge (sodiation). Red squares indicate the area where the charge storage characteristics changes from a linear to an S-shaped increase, enlarged for TiO_{2-x}-A in b), TiO_{2-x}-R d), and MoO_{2+x} f).

NaO_2 upon desodiation,[13] in combination with significant self-improving charge storage characteristics. The nature of self-improving charge storage increase has been found to depend on the C-rate, on the time (i.e., the number of cycles), as well as on the crystal structure of the active material.[12]

2.2. Galvanostatic Cycling with Potential Limitation

As the long-term cyclability is essential to initiate and study the self-improving charge storage characteristics, GCPL was performed in the voltage range of 0.1–3 V at seven different current densities for all electrode materials, starting from 117 µA (51.8 µA cm^{-2}), down to 1.2 µA (0.5 µA cm^{-2}). The specific gravimetric capacities in the GCPL curves (Figure 3) are shown with respect to the active oxide mass of the electrode (the surface normalized graphs can be seen in Figure S4, Supporting Information).

Figure 3a shows the specific gravimetric charge–discharge capacities of TiO_{2-x}-A, ranging from initially 37 mAh g^{-1} (3.5 µAh cm^{-2}), at a constant current of 117 µA (51.8 µA cm^{-2}), to about 107 mAh g^{-1} (10 µAh cm^{-2}) in the last cycle, at a constant current of 1.2 µA (0.5 µA cm^{-2}). The capacity increase measured for TiO_{2-x}-A (Figure 3a) is concurrent with our previous findings for anatase TiO_{2-x} NTs.[12] At high currents (fast charge–discharge rates) of 117 µA to 6 µA, a linear capacity increase is observed. Between 24 µA and 6 µA, the strongest increase is measured, with a capacity increase of 6.83 mAh g^{-1} over 50 cycles at a current of 24 µA, 7.15 mAh g^{-1}

over 50 cycles at a current of 12 μA, and 10.28 mAh g^{-1} over 50 cycles at a current of 6 μA, respectively. At a current of 2.4 μA, a progressive increase of the self-improvement, and a corresponding change from a linear to an S-shaped increase, best described by a logistic growth function, occurs (Figure 3b). Between 6 μA and 2.4 μA, a certain threshold value is reached, altering the kinetics in the surface film formation process.[13] The total capacity improvement during logistic growth equals 6.91 mAh g^{-1} over 10 cycles only (cycle 251 to 260, Figure 3b), at a current of 2.4 μA (1.1 μA cm^{-2}). At an even lower current of 1.2 μA (0.5 μA cm^{-2}), the specific capacity finally plateaus at 108.3 mAh g^{-1} after 310 cycles. The self-improvement of the capacity in the TiO_{2-x}-A electrodes is sustained in the subsequent cycles, demonstrating good cycling stability. Sustainable long-term galvanostatic cycling stability over 500 cycles has been previously reported for carburized anatase TiO_{2-x}-C NTs. Reversible sodiation/desodiation capacities of about 60 mAh g^{-1} have been measured at high current rates of 20C (12 A g^{-1}).[12]

The charge–discharge characteristics of TiO_{2-x}-R (Figure 3c) are similar compared with TiO_{2-x}-A, with an overall lower, final specific capacity of 83.5 mAh g^{-1} after 310 cycles. While the initial capacity is quite low with only 8.34 mAh g^{-1} after the first 50 cycles, the specific capacity increases by 28.1 mAh g^{-1} between cycle 200 and 290 at a current of 6 and of 2.4 μA, respectively. Again, at a current of 2.4 μA, a progressive increase in self-improvement occurs, and the curve follows an S-shape instead of a linear increase (Figure 3d). The lower final gravimetric capacity can be partly attributed to the difference in density between anatase (3.84 g cm^{-3}) and rutile (4.24 g cm^{-3}) TiO_2. In additon, from the CV response for the aged TiO_{2-x}-R at slow scan rates (1 mV s^{-1}, Figure 2c), more complex surface chemistry can be inferred, suggesting the presence of an additional species formed during cycling, that may not contribute to the overall reversible specific Na-ion storage capacity.

The nature of the chemical bond in metal oxides is related to the local structure, such as the M–O interatomic distance and the coordination number around the M-atom. In the TiO_2 (anatase and rutile) and MoO_2 oxide structure, a metal atom is surrounded by oxygen atoms to form a MO_6 octahedron.[26] Calculations showed that the chemical interactions operating between atoms in MO_6 octahedra vary with the composition and density of the oxides. The difference in atomization energy for O is larger in anatase than in rutile, although the local structure (M–O interatomic distance and the coordination number around the M atom) is almost similar between them. Furthermore, these calculations indicate that the relative stabilities of oxygen vacancies at surface and subsurface sites are significantly higher at subsurface than at surface sites in the case of anatase surfaces, whereas bridging oxygen sites are favored for O vacancies at rutile TiO_2.[26] For anatase TiO_2, calculations of O vacancy diffusion pathways show that the energy barrier to diffuse from surface-to-subsurface sites is sufficiently low, which causes a rapid equilibration of vacancy distribution.[19] This, in turn, facilitates initial Na_2O and subsequent Na_2O_2 formation which heavily depends on the O diffusion characteristics of the material.[13]

The charge–discharge behavior of MoO_{2+x} (Figure 3f,e) shows significant differences compared with TiO_{2-x}-A and TiO_{2-x}-R. The progressive increase in the self-improving charge storage characteristics already occurs at the highest current of 117 μA (51.8 μA cm^{-2}), followed by a further steep but more linear increase at a current of 59 μA (26.1 μA cm^{-2}). The total specific capacity increase between cycle 20 and cycle 80 amounts to 22.08 mAh g^{-1} (Figure 3f). Different from TiO_{2-x}-A and TiO_{2-x}-R, this self-improvement of the capacity is retained in the subsequent cycles at low currents of 24, 12, and 6 μA, but does not increase further. At even lower currents of 2.4 μA (1.1 μA cm^{-2}), the specific capacity starts to decrease again (Figure 3e), similar to the charge–discharge characteristics of common intercalation materials.[27,28] This, in fact, would support the idea of possible sodiation of the topmost MoO_2 layers by an intercalation reaction at very slow sodiation rates, according to Equation (1), as previously discussed, and is also indicated by the ill-defined, broad redox wave at slow scan rates (i.e., at 1 mV s^{-1}, Figure 2e).[17,24] At fast sodiation rates, that is, high currents, the kinetically fast conversion reactions to Na_2O or Na_2O_2 may dominate, according to Equation (3). In addition, dissolution of NaO_2 to Na_2O_2 and Na_2O_2 dihydrate may also contribute to the capacity decrease observed.[14–16]

MoO_2 is characterized by a significantly lower cohesive energy of the metal oxide with 9.05 eV, compared with 9.93 eV, for TiO_2.[26] The cohesion energy, being the sum of the atomization energies of metal and oxygen atom in the MO_6 octahedron, reflects the local, as well as the average structure. Values vary, depending on the type (vertex, edge or face sharing) of MO_6 octahedron, and also change with the overall density of the metal oxides. Thus, the cohesion energy is a measure for the stability of the oxide, which is, in light of our previous work, next besides electronic conductivity, a crucial parameter for potential surface film formation.[12,13] MoO_2 demonstrates already at high sodiation rates (i.e., high C-rates) a considerable self-improving effect (compare cycle 20–80 in Figure 3f). For TiO_2 anatase and rutile, the most significant film formation occurs at slow sodiation rates, between cycle 230 and 270 (Figure 3b,d). The reason for this difference in the metal oxides can be found in the high, metal-like, electronic conductivity of MoO_2 with about 8.8×10^{-5} Ω cm at 300 K.[29] TiO_2, on the other hand, is a wide-bandgap semiconductor with a bandgap of rutile and anatase TiO_2 at 3.03 and 3.20 eV, respectively.[30,31] Reports on the resistivities of polycrystalline bulk anatase range from 10^2 to 10^7 Ω cm at 300 K.[32] These differences are clearly reflected in the potential-dependent electrochemical impedance response of the three systems (Figure S5, Supporting Information).

2.3. X-ray Photoelectron Spectroscopy

To assess the nature of the compounds formed upon sodiation/desodiation, quasi in situ XPS analysis[21] of the different oxide electrodes before (Figure S6, Supporting Information) and after (ex situ, Figure S7, Supporting Information) battery cycling are recorded. Therefore, the samples were immersed from the electrolyte under potential control at 0.1 V after cycling and transferred to the XPS without contact to ambient air, in order to preserve the state of the electrodes after the final sodiation process. The exact transfer procedure is described in the study by Watschinger et al.[33]

XPS survey spectra of TiO_{2-x}-A and MoO_{2+x} (Figure S7, Supporting Information) after sodiation show the presence of S, C, N, and F, which are impurities originating from the electrolyte. The weak Ti 2*s* and Ti 2*p* peak intensities indicate the presence of a relatively homogeneous surface layer, while the distinctly visible Mo 3*d* signal (Figure S7b, Supporting Information), compared with the weak Ti 2*p* signal (Figure S7a, Supporting Information), at 233 eV, suggests that the surface film does not form a closed layer and a rather thin film of MoO_{2+x}. This can be further confirmed by ex situ, top-view SEM imaging (Figure S8, Supporting Information), showing continuous surface clusters on the sodiated TiO_{2-x}-A electrodes covering the TiO_{2-x}-A surface (Figure S8b, Supporting Information) quite homogeneously. In case of aged MoO_{2+x} electrodes, significant parts of the surface are not covered by a film (Figure S8d,f, Supporting Information). Both survey spectra show distinctive peaks of the Na 1*s*, Na Auger KLL, and O 1*s* signals, which are attributed to Na_xO_y and Na_2CO_3 species and are in accordance with areal, ex situ EDX analysis (Figure S9, Supporting Information). To more quantitatively assess the nature of the compounds formed upon sodiation/desodiation, high-resolution C 1*s* (**Figure 4**) and O 1*s* (**Figure 5**) spectra are recorded and fitted.

Figure 4 shows ex situ emersion, high-resolution C 1*s* spectra of TiO_{2-x}-A, TiO_{2-x}-R, and MoO_{2+x} before (surface) and after 20 s of argon sputtering. For all samples, three different species

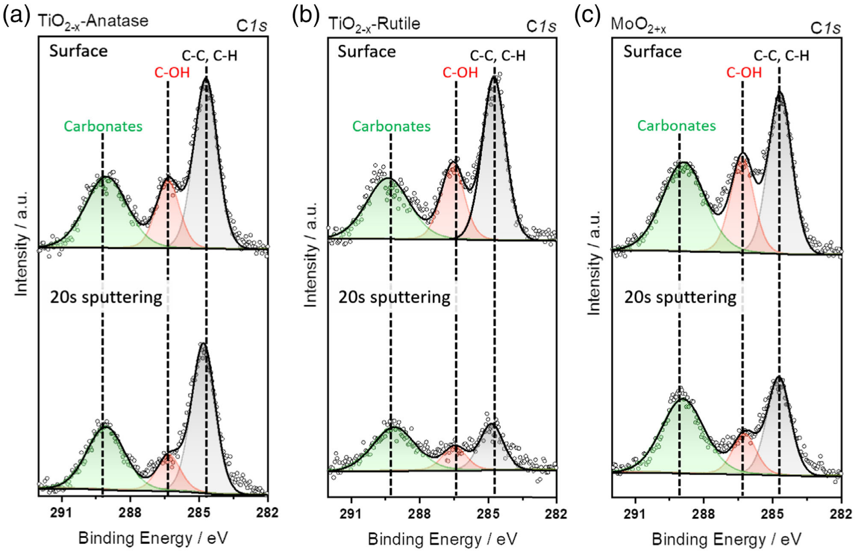

Figure 4. Elemental composition of the electrodes after sodiation. Quasi in situ high-resolution C1s XPS spectra of a) TiO_{2-x}-A, b) TiO_{2-x}-R, and c) MoO_{2+x} before (surface) and after 20 s of argon sputtering.

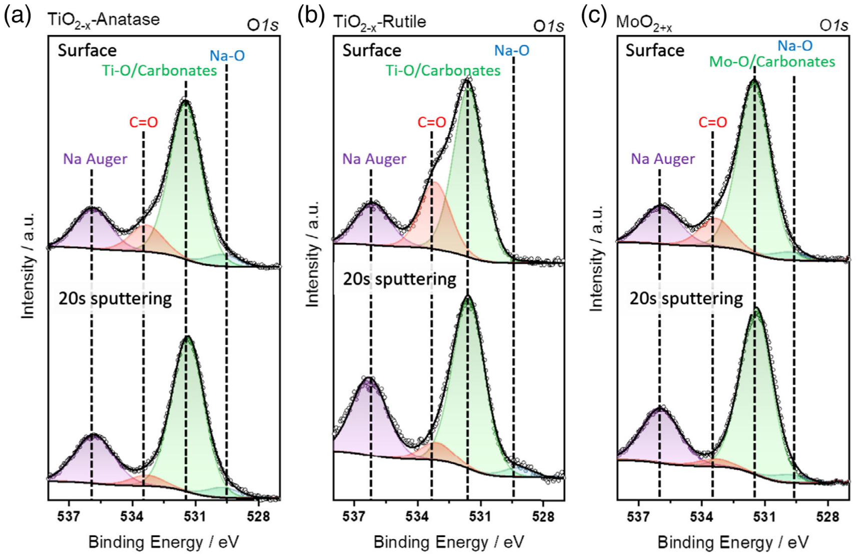

Figure 5. Elemental composition of the electrodes after sodiation. Quasi in situ high-resolution O1s XPS spectra of a) TiO_{2-x}-A, b) TiO_{2-x}-R, and c) MoO_{2+x} before (surface) and after 20 s of argon sputtering.

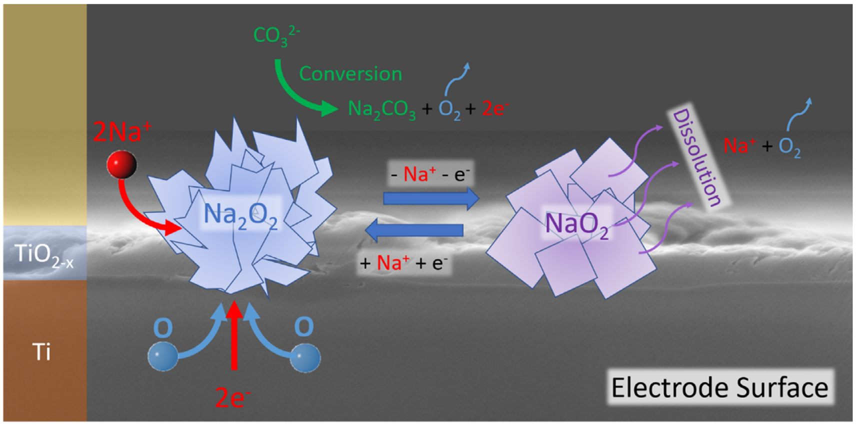

Figure 6. Schematic diagram of the envisaged sodiation and desodiation reactions. Initial formation of Na_2O_2 on top of the oxide surface film by the reduction of lattice oxygen and its subsequent conversion to NaO_2. Possible, parasitic side reactions are shown by the conversion of Na_2O_2 to Na_2CO_3 and the dissolution of NaO_2 in combination with O_2 release into the electrolyte solution.

sum up to the overall envelope spectrum, that is, hydrocarbons (C–C, C–H) at ≈285 eV, surface OH groups (C–OH) at ≈286.5 eV, and carbonates at ≈290 eV. Upon 20 s of sputtering the areal percentages of both, the hydrocarbons (C–C, C–H) and surface OH groups (C–OH), decrease, while the carbonate peak, located at 289 eV, remains almost constant, with 34.8% at the surface and 35.6% after 20 s argon sputtering. Since a thin layer of C–C-, C–H-, and C–OH-containing species is also present on the pristine electrodes, and these signals have almost disappeared after 20 s of argon sputtering (Figure S10, Supporting Information), they are assigned to adventitious carbon.

The O 1*s* high-resolution spectra after sodiation (Figure 5) were deconvoluted prior to and after 20 s of sputtering. This allows to unambiguously differentiate between metal oxide and carbon-bound oxygen species. Overall, four different species contribute to the high-resolution spectrum, the Na metal oxide component at ≈530 eV, carbonates at ≈532 eV, the organic carbon-bound oxygen (C–O) at ≈534 eV, and the Na KLL Auger line at ≈536 eV. The pristine O 1*s* spectra show only oxide and carbonate compounds (Figure S11, Supporting Information).

For the electrodes after sodiation, the amount of Na and metal–oxide species slightly increases upon sputtering, whereas the carbon-bound oxygen vanishes. This agrees well with previous studies, showing that the surface of the electrodes is covered with organic species (from the decomposition of the electrolyte), whereas the bulk of the acicular film mainly comprises Na_2O_2 and Na_2CO_3.[13] Whether both, Na_2O_2 and NaO_2 are present or only Na_2O_2 can hardly be determined, due to the similar peak positions of 530.9 eV (Na_2O_2) and 529.7 eV (NaO_2), respectively. Thermodynamic calculations show that the corresponding reduction potentials of Na_2O_2 (2.33 V) and NaO_2 (2.27 V), calculated at 298 K and an oxygen partial pressure of 10^5 Pa, are very similar between the two species. Therefore, it is likely that either Na_2O_2 or NaO_2 can be formed upon sodiation and desodiation (**Figure 6**).[34]

In summary, for all three metal oxides under study, the surface film seems to be of similar composition. The topmost layers are characterized by carbon-containing species, whereas inorganic species (mainly Na_2O_2 and Na_2CO_3) apparently dominate the bulk of the surface film.

3. Conclusion

Three different electrode materials, TiO_{2-x}-A, TiO_{2-x}-R, and MoO_{2+x}, were investigated in terms of their Na-ion storage characteristics. Electrochemical characterization by CV shows distinctive differences in the current response between initial, that is, after synthesis, and aged electrodes. The latter are characterized by a significant current increase and well-defined redox reactions for TiO_{2-x}-A and TiO_{2-x}-R. Long-term GCPL measurements reveal, for all three materials under investigation, a substantial capacity increase upon cycling. Interestingly, while for TiO_{2-x}-A and TiO_{2-x}-R, significant self-improvement in the charge storage capacity starts only at low currents of 24 μA and below; this is markedly different for MoO_{2+x}. For MoO_{2+x}, and self-improvement in the charge storage capacity is observed at the highest current of 117 μA. This difference in the kinetics is explained by the high, metal-like, electronic conductivity of MoO_2 and by the significantly lower cohesive energy of the metal oxide in MoO_{2+x}, compared with TiO_{2-x}-A and TiO_{2-x}-R, resulting in enhanced oxygen diffusivity. As the observed capacity increase is related to the formation of a Na-containing surface film, with Na_2O_2, NaO_2 and Na_2CO_3, forming the main constituents, the oxygen diffusion in the bulk oxide is important for the initial film growth. Na_2O_2, NaO_2, and Na_2CO_3 are found to be present in all three transition metal oxide surface films. The proposed surface chemistry seems to be a common scheme for Na-ion storage at transition metal oxide surfaces, in general, improving both, the specific gravimetric Na-ion storage capacity and the sodiation/desodiation rate capability. To further exploit these findings in Na-ion and Na–oxygen batteries, sufficient oxygen diffusion within the bulk metal oxide lattice in combination with good electronic conductivity is of vital importance for effective surface film formation.

4. Experimental Section

Synthesis: The synthesis of TiO_{2-x}-A and TiO_{2-x}-R was performed in several steps. In the preparation process, the metallic titanium disk (Advent, 99.6%) with a diameter of 18 mm and a thickness of 1 mm was polished with SiC grinding papers (P1200, P2500, and P4000 from Buehler) three times for five minutes each. After every polishing step, the sample was cleaned in ethanol in an ultrasonic bath for 5 min.[35] The next step was electrochemical oxidation to an amorphous TiO_2 using a two-electrode setup with a copper plate as current collector, the titanium disc as a working electrode, a platinum net as the counter electrode (CE), and 0.1 M H_2SO_4 as electrolyte. After cell assembly, a constant potential of 20 V was applied for 60 min with an initial voltage ramp of 1 V s^{-1}.[35,36]

The third and last step was phase transition from the amorphous TiO_2 into the anatase phase/rutile phase, which took place in a Carbolite furnace with quartz tube reactor. Initially, the reactor was flushed for 90 min at room temperature with 600 sccm Ar to remove the ambient air inside. Then, the Ar flow was decreased to 200 sccm, which remained constant until the end of the annealing process. The temperature was stepwise increased from room temperature up to 200 °C in 20 min, up to 300 °C in 20 min, and up to 400 °C in 33 min for the anatase phase and from room temperature up to 650 °C in 251 min for the rutile phase. The final temperature of 400 °C and 650 °C for anatase and rutile was kept constant for 300 min and 1440 min, respectively, to ensure complete phase transition. Subsequently, the furnace was cooled down to room temperature.[37]

The synthesis of MoO_{2+x} was carried out by a radio frequency magnetron-based physical vapor deposition (PVD). A comprehensive review of the entire apparatus with its individual components was made by Götsch et al.[38] The base pressure of this setup was 2×10^{-6} mbar. The oxygen/Ar ratio of 1:100 was adjusted by setting the pressures to $1.00 \pm 0.05 \times 10^{-4}$ mbar and $1.00 \pm 0.05 \times 10^{-2}$ mbar for oxygen and Ar, respectively. The magnetron was slowly ramped up to a final output of 40 W. In order to prevent impurities on the surface of the Mo target (99.95%, Kurt J. Lesker) from affecting our synthesis, Ar sputtering was performed for 30 min. With the shutter closed before the actual deposition started, the deposition time was 1 h.[39]

Raman: The characterizations of TiO_{2-x}-A and TiO_{2-x}-R were performed by Raman spectroscopy using a WiTec alpha 300 Raman microscope with an objective providing a 40× magnification including a confocal laser scanning microscope with a wavelength of 532 nm. The integration time for each measurement was about three minutes and the applied grid had a mesh size of 1800 lines/mm. For the measurement control and data evaluation, the software WiTec Control 5.1 was used.

XRD: XRD analysis was performed on a Siemens D5000 Diffractometer. Diffractograms were acquired between 25 and 55 degrees (2 theta) with a step size of 0.02 degrees (2 theta) and an acquisition time of 1 s per step.

SEM: To determine the mass fraction of TiO_{2-x}-A, TiO_{2-x}-R, and MoO_{2+x}, cross sections were prepared using a Jeol IB-19 530 CP Ar plasma etcher and subsequently, imaged by a Jeol JSM-7610F field-emission SEM. For that, the MoO_{2+x} layer was sputtered onto a 0.1 mm-thick copper sheet. The electrochemical oxidation of TiO_{2-x}-A was realized with a 0.125 mm-thick titanium foil instead of the 1 mm-thick titanium disc. Then, each of the samples was put in the path of a 2 mm-broad beam of stationary Ar plasma. A shielding plate protected the samples and only the part protruding from the edge of the mask was milled away. This resulted in a clean polished cross section. The samples were cut from the backside to protect the surface of the thin films and hence, to improve the cutting edge of the film. The clean cutting edge is indispensable to determine the thickness correctly. For mass calculation, five thicknesses were measured from each of the two SEM images (Figure 1) at different positions and the average value was calculated, which equaled, in the case of TiO_{2-x}-A and TiO_{2-x}-R 248 ± 28 nm and in the case of MoO_{2+x}, 209 ± 10 nm. The oxide mass was calculated by multiplying the oxide volume by the corresponding oxide density, being 3.84, 4.24, and 6.40 g cm^{-3}, respectively.

X-ray Photoelectron Spectroscopy: All postmortem samples were transported by help of an air-tight cell and a glovebox flanged to the preparation chamber of the XPS.[33] The characterizations of the MoO_{2+x} was performed using a Thermo MultiLab 2000 XPS with a hemispherical energy analyzer and a monochromatized Al Kα X-ray source (1486.6 eV). More precisely the ratio of the Mo(IV)-oxide and the Mo(VI)-oxide after the synthesis and the composition of the surface film after cycling at potentials of 0.1 V were determined. The take-off angle in XPS measurements was 0 relative to the surface normal and a monochromatized Al Kα X-ray source (1486.6 eV) was used. The ion gun (3 kV) inside the analysis chamber, was used for depth profiling analysis by Ar^+ etching. High resolution spectra were recorded for the Ti 2*p*, C 1*s*, O 1*s* Na 1*s*, S 2*s* and F 1*s* regions with a step size of 0.02 eV and a dwell time of 0.2 s. Quantitative analysis was performed using CasaXPS software (version 2.3.16). A flood gun was used for charge compensation. All spectra were shifted to the Ti 2*p* region for calibration of the binding energy scale, with respect to Ti 2*p* 3/2 Ti(IV) region to 458.7 eV. All relevant shifted peak positions and widths of MoO_{2+x} and TiO_{2-x}-A are given in Table S1, Supporting Information.

Electrochemistry: For electrochemical characterization, a three-electrode EL cell setup (ECC ref cell) was used. Therefore a 0.1–0.5 mm-thick sodium metal foil (99.9%) counter electrode (CE) having a diameter of 16 mm and a Na reference electrode (RE) were prepared and mounted in the PEEK sleeve which in turn was placed into the stainless steel cell base. The glass fiber separator (EL-Cell, 18 × 1.55 mm) was inserted into the PEEK sleeve, and 500 µL of 99.9% pure electrolyte, containing 1 M Na FSI (Bis(fluorosulfonyl)imide) in 1:1 V V^{-1} ethylene carbonate:dimethyl carbonate from Solvionic, was added. The whole assembling process was carried out in a glovebox filled with Ar, containing contents of H_2O and O_2 below 0.1 ppm, due to the reactivity of MoO_{2+x} and the electrolyte with oxygen and the hazardous reactivity of the used sodium with oxygen and humidity, respectively. To investigate the surface with ex situ XPS, punched, double-spaced separators were put in the cell to avoid impurities of the surface from the separator. The actual measurements were performed using a BioLogic VMP3 potentiostat.

Supporting Information

Supporting Information is available from the Wiley Online Library or from the author.

Acknowledgements

The authors gratefully acknowledge the support of the Austrian Science Foundation (FWF) within the FWF project P29645 and P34233. D. W. is a recipient of DOC fellowship of the Austrian Academy of Sciences (ÖAW) at the Institute of Physical Chemistry.

Conflict of Interest

The authors declare no conflict of interest.

Data Availability Statement

The data that support the findings of this study are available from the corresponding author upon reasonable request.

Keywords

batteries, Na ions, oxides, self-improvement, surface films

Received: July 11, 2022
Revised: September 20, 2022
Published online:

[1] O. Hoegh-Guldberg, D. Jacob, M. Taylor, T. Guillén Bolaños, M. Bindi, S. Brown, I. A. Camilloni, A. Diedhiou, R. Djalante, K. Ebi, F. Engelbrecht, J. Guiot, Y. Hijioka, S. Mehrotra, C. W. Hope, A. J. Payne, H.-O. Pörtner, S. I. Seneviratne, A. Thomas, R. Warren, G. Zhou, *Science* **2019**, *365*, eaaw6974.

[2] E. Byers, M. Gidden, D. Leclère, J. Balkovic, P. Burek, K. Ebi, P. Greve, D. Grey, P. Havlik, A. Hillers, N. Johnson, T. Kahil, V. Krey, S. Langan, N. Nakicenovic, R. Novak, M. Obersteiner, S. Pachauri, A. Palazzo, S. Parkinson, N. D. Rao, J. Rogelj, Y. Satoh, Y. Wada, B. Willaarts, K. Riahi, *Environ. Res. Lett.* **2018**, *13*, 055012.

[3] J. Tollefson, *Nature.* **2019**, *574*, 17.

[4] J.-M. Tarascon, M. Armand, *Nature.* **2001**, *414*, 359.

[5] K. Amine, R. Kanno, Y. Tzeng, *MRS Bull.* **2014**, *39*, 395.

[6] G. Martin, L. Rentsch, M. Höck, M. Bertau, *Energy Storage Mater.* **2017**, *6*, 171.

[7] M. D. Slater, D. Kim, E. Lee, C. S. Johnson, *Adv. Funct. Mater.* **2013**, *23*, 947.

[8] C. Vaalma, D. Buchholz, M. Weil, S. Passerini, *Nat. Rev. Mater.* **2018**, *3*, 18013.

[9] P. K. Nayak, L. Yang, W. Brehm, P. Adelhelm, *Angew. Chem., Int. Ed.* **2018**, *57*, 102.

[10] J. Tang, X. Peng, T. Lin, X. Huang, B. Luo, L. Wang, *EScience* **2021**, *1*, 203.

[11] S. Ye, L. Wang, F. Liu, P. Shi, Y. Yu, *EScience* **2021**, *1*, 75.

[12] E. Portenkirchner, D. Werner, S. Liebl, D. Stock, A. Auer, J. Kunze-Liebhäuser, *ACS Appl. Energy Mater.* **2018**, *1*, 6646.

[13] E. Portenkirchner, S. Rommel, L. Szabados, C. Griesser, D. Werner, D. Stock, J. Kunze-Liebhäuser, *Nano Sel.* **2021**, *2*, 1533.

[14] S. Lau, L. A. Archer, *Nat. Energy.* **2016**, *1*, 16019.

[15] J. Kim, H. Park, B. Lee, W. M. Seong, H.-D. Lim, Y. Bae, H. Kim, W. K. Kim, K. H. Ryu, K. Kang, *Nat. Commun.* **2016**, *7*, 10670.

[16] H. Yadegari, Q. Sun, X. Sun, *Adv. Mater.* **2016**, *28*, 7065.

[17] X. Zhao, Y. Zhao, Y. Yang, Z. Liu, H.-E. Wang, J. Sui, W. Cai, *New J. Chem.* **2018**, *42*, 14721.

[18] B. P. Uberuaga, X.-M. Bai, *J. Phys. Condens. Matter.* **2011**, *23*, 435004.

[19] H. Cheng, A. Selloni, *Phys. Rev. B.* **2009**, *79*, 092101.

[20] V. Guidi, M. C. Carotta, M. Ferroni, G. Martinelli, M. Sacerdoti, *J. Phys. Chem. B* **2003**, *107*, 120.

[21] A. Foelske-Schmitz, *Encyclopedia of Interfacial Chemistry*, Elsevier, Amsterdam, Boston **2018**, pp. 591–606, https://doi.org/10.1016/B978-0-12-409547-2.11549-5.

[22] C. Rüdiger, M. Favaro, C. Valero-Vidal, L. Calvillo, N. Bozzolo, S. Jacomet, C. Hejny, L. Gregoratti, M. Amati, S. Agnoli, G. Granozzi, J. Kunze-Liebhäuser, *Phys. Chem. Chem. Phys.* **2016**, *18*, 9220.

[23] J. Jiang, W. Yang, H. Wang, Y. Zhao, J. Guo, J. Zhao, M. Beidaghi, L. Gao, *Electrochim. Acta* **2017**, *240*, 379.

[24] L. C. Yang, Q. S. Gao, Y. Tang, Y. P. Wu, R. Holze, *J. Power Sources* **2008**, *179*, 357.

[25] X. Hu, W. Zhang, X. Liu, Y. Mei, Y. Huang, *Chem. Soc. Rev.* **2015**, *44*, 2376.

[26] Y. Shinzato, Y. Saito, M. Yoshino, H. Yukawa, M. Morinaga, T. Baba, H. Nakai, *J. Phys. Chem. Solids* **2011**, *72*, 853.

[27] E. de la Llave, V. Borgel, K. Park, J. Hwang, Y. Sun, P. Hartmann, F.-F. Chesneau, D. Aurbach, *ACS Appl. Mater. Interfaces* **2016**, *8*, 1867.

[28] M. Goktas, C. Bolli, E. J. Berg, P. Novák, K. Pollok, F. Langenhorst, M. V. Roeder, O. Lenchuk, D. Mollenhauer, P. Adelhelm, *Adv. Energy Mater.* **2018**, *8*, 1702724.

[29] Y. Shi, B. Guo, S. A. Corr, Q. Shi, Y.-S. Hu, K. R. Heier, L. Chen, R. Seshadri, G. D. Stucky, *Nano Lett.* **2009**, *9*, 4215.

[30] D. O. Scanlon, C. W. Dunnill, J. Buckeridge, S. A. Shevlin, A. J. Logsdail, S. M. Woodley, C. R. A. Catlow, M. J. Powell, R. G. Palgrave, I. P. Parkin, G. W. Watson, T. W. Keal, P. Sherwood, A. Walsh, A. A. Sokol, *Nat. Mater.* **2013**, *12*, 798.

[31] V. Pfeifer, P. Erhart, S. Li, K. Rachut, J. Morasch, J. Brötz, P. Reckers, T. Mayer, S. Rühle, A. Zaban, I. Mora Seró, J. Bisquert, W. Jaegermann, A. Klein, *J. Phys. Chem. Lett.* **2013**, *4*, 4182.

[32] K. Lee, A. Mazare, P. Schmuki, *Chem. Rev.* **2014**, *114*, 9385.

[33] M. Watschinger, K. Ploner, D. Winkler, J. Kunze-Liebhäuser, B. Klötzer, S. Penner, *Rev. Sci. Instrum.* **2021**, *92*, 024105.

[34] K. Song, D. A. Agyeman, M. Park, J. Yang, Y.-M. Kang, *Adv. Mater.* **2017**, *29*, 1606572.

[35] A. Auer, N. S. W. Jonasson, D. H. Apaydin, A. I. Mardare, G. Neri, J. Lichtinger, R. Gernhäuser, J. Kunze-Liebhäuser, E. Portenkirchner, *Energy Technol.* **2017**, *5*, 2253.

[36] L. Calvillo, D. Fittipaldi, C. Rüdiger, S. Agnoli, M. Favaro, C. Valero-Vidal, C. Di Valentin, A. Vittadini, N. Bozzolo, S. Jacomet, L. Gregoratti, J. Kunze-Liebhäuser, G. Pacchioni, G. Granozzi, *J. Phys. Chem. C* **2014**, *118*, 22601.

[37] A. Auer, S. Dominik, E. Portenkirchner, J. Kunze-Liebhäuser, *ACS Appl. Energy Mater.* **2018**, *1*, 1924.

[38] T. Götsch, E.-M. Wernig, B. Klötzer, T. Schachinger, J. Kunze-Liebhäuser, S. Penner, *Rev. Sci. Instrum.* **2019**, *90*, 023902.

[39] M. Sook Oh, B. Seob Yang, J. Ho Lee, S. Ha Oh, U. Soo Lee, Y. Jang Kim, H. Joon Kim, M. Soo Huh, *J. Vac. Sci. Technol., A* **2012**, *30*, 31501.